PCCP

Cite this: *Phys. Chem. Chem. Phys.*, 2012, **14**, 9936–9941

www.rsc.org/pccp

PAPER

Temperature dependence of phonon modes, dielectric functions, and interband electronic transitions in Cu_2ZnSnS_4 semiconductor films

Wenwu Li, Kai Jiang, Jinzhong Zhang, Xiangui Chen, Zhigao Hu,* Shiyou Chen, Lin Sun and Junhao Chu

Received 15th April 2012, Accepted 22nd May 2012
DOI: 10.1039/c2cp41209h

The quaternary semiconductor Cu_2ZnSnS_4 (CZTS) has attracted a lot of attention as a possible absorber material for solar cells due to its direct bandgap and high absorption coefficient. In this study, photovoltaic CZTS nanocrystalline film with a grain size of about 10 nm has been grown on a *c*-plane sapphire substrate by radio-frequency magnetron sputtering. With increasing the temperature from 86 to 323 K, the A_1 phonon mode shows a red shift of about 9 cm^{-1} due to the combined effects of thermal expansion and the anharmonic coupling to the other phonons. Optical and electronic properties of the CZTS film have been investigated by transmittance spectra in the temperature range of 8–300 K. Near-infrared-ultraviolet dielectric functions have been extracted with the Tauc–Lorentz dispersion model. The fundamental band gap E_0, and higher-energy critical points E_1 and E_2 are located at 1.5, 3.6, and 4.2 eV, respectively. Owing to the influences of electron–phonon interaction and the lattice expansion, the three interband transitions present a red shift trend with increasing temperature. It was found that the absorption coefficient in the visible region increases due to the modifications of electronic band structures. The detailed study of the optical properties of CZTS film can provide an experimental basis for CZTS-based solar cell applications.

1 Introduction

High efficiencies combined with the potential for low cost and large scale production make the studied technology a serious candidate for finally penetrating the photovoltaic market.[1] Recently, the quaternary semiconductor Cu_2ZnSnS_4 (CZTS), whose crystal structure and optical properties are similar to those of $Cu(In,Ga)Se_2$, has attracted considerable attention for its technological applications in photovoltaic devices.[2–4] With the advantages of a near-optimal band gap ($\sim$1.5 eV),[5] high absorption coefficient ($>10^4$ cm^{-1}),[6] earth-abundant elements, and low cost, CZTS has been considered as one of the most promising photovoltaic absorber materials. Much effort has been made on the investigations of the diverse properties of CZTS.[5–8] Recently, Persson reported the electronic and optical properties of CZTS and $Cu_2ZnSnSe_4$ (CZTSe), and found that CZTS has a larger band gap but a lower high frequency dielectric constant.[5] Gunawan *et al.* investigated the temperature dependent electrical characteristics of the $Cu_2ZnSn(S,Se)_4$ solar cell and found that the device has very low minority carrier lifetimes, and high series resistance at low temperature.[9] Moreover, it was reported that the CZTS solar cell with a high power conversion efficiency of up to 6.8% has been achieved by thermal evaporation and sputtering.[10] Also, Todorov *et al.* reported a record of 9.66% conversion efficiency for the $Cu_2ZnSn(S,Se)_4$-based solar cell using the spin-coating method.[3] According to the photon balance calculations of Shockley–Queisser, CZTS is expected to have a theoretical efficiency of more than 30%.[11] Although the above concept has already been accepted, the critical issue is to answer how the electronic band structure and optical absorption of CZTS layer are from the experimental viewpoint. In order to further improve the optoelectronic device performance, it is necessary to understand more about the physical properties and underlaying mechanism of CZTS material as a solar cell absorber layer.

As of now, most of the studies have focused on the structure and electrical properties of CZTS.[4,12,13] It should be emphasized that the optical properties of the absorber materials play an important role in determining the efficiency of photovoltaic devices. Although the optical and transport properties have been theoretically studied,[5,14] there are few experimental investigations on interband electronic transition of CZTS materials, especially for the ultraviolet-infrared dielectric functions. The singularities in the imaginary part of dielectric functions can be assigned to the specific interband transitions. On the other hand, the optical band gap (OBG) is one of

Key Laboratory of Polar Materials and Devices, Ministry of Education, Department of Electronics Engineering, East China Normal University, Shanghai 200241, People's Republic of China. E-mail: zghu@ee.ecnu.edu.cn; Fax: +86-21-54345119; Tel: +86-21-54345150

the fundamentally and technologically important characteristics for solar cell applications. One crucial factor of solar cells is the mismatch of their absorption to the terrestrial solar spectrum, and an optimal band gap can enhance the number of photons absorbed. Moreover, the temperature dependence of the OBG from the interband transitions can provide important information about the electron–phonon interactions and collective excitations of semiconductors. In recent experiments, the OBG values of the CZTSe compound are scattered from about 1.0 eV to 1.5 eV using the linear extrapolation method.[15] It is well-known that films can be deposited directly on diversified substrates and are expected to yield better sensitivity and faster responses than the equivalent bulk single crystal. Therefore, the temperature-dependent OBG of CZTS film should be thoroughly studied in order to exploit its potential applications in photovoltaic devices. Note that optical transmittance spectroscopy is widely accepted and applied in the case of transparent substrates, which can determine the absorption edge, optical constants, and OBG. Furthermore, the Raman scattering spectral technique can provide some invaluable information on the structure, phase purity, chemical composition, and lattice dynamics. Correspondingly, it can distinguish the stannite or kesterite structures from other secondary phases that are formed during CZTS growth.

In this paper, the optical properties of the CZTS film have been investigated by Raman scattering and transmittance spectral techniques. The temperature dependent OBG and dielectric functions have been extracted by fitting the transmittance spectra with the dispersion model. The effects from temperature on the phonon modes and electronic band structures of the CZTS film have been discussed in detail.

2 Experimental details

2.1 Fabrication of the CZTS film

The CZTS film was prepared by radio-frequency (RF) magnetron sputtering deposition in an argon atmosphere (1.6 Pa). The double-side polished *c*-plane sapphire substrate, which was selected for the ultraviolet transmittance measurements, was ultrasonically cleaned in acetone, distilled water, and ethanol, and dried in a nitrogen gas stream before being put into the vacuum chamber. The CZTS target with a diameter of 50 mm was obtained using a conventional solid-state reaction sintering of highly pure cuprous sulfide (Cu_2S), zinc sulfide (ZnS), tin bisulfide (SnS_2), and sulfur (S) powders. The substrate was rotated at 10 rpm to ensure uniformity of film deposition. The target was presputtered for several minutes to clean their surfaces. After the deposition, the film was annealed at 400 °C in an argon atmosphere for 1 h.

2.2 XRD, AFM, Raman scattering and transmittance spectra measurements

The crystalline structure of the CZTS film was analyzed by X-ray diffraction (XRD) using Cu Ka radiation (D/MAX-2550 V, Rigaku Co.). The surface morphology was investigated by atomic force microscopy (AFM) with the contacting mode in areas of 2 × 2 μm^2 (Digital Instruments Dimension 3100, Veeco). Temperature-dependent Raman scattering experiments were carried out by a Jobin-Yvon LabRAM HR 800 micro-Raman spectrometer and a THMSE 600 heating/cooling stage (Linkam Scientific Instruments) in the temperature range from 86 to 323 K. The set-point stability is better than 0.5 K. A laser with a wavelength of 488 nm was used as the excitation source with a power of 20 mW and the spectral resolution was better than 1 cm^{-1}. The laser beam was focused through a 50× microscope with a numerical aperture of 0.35 and a working distance of 18 mm. An air-cooled charge coupled device (CCD) was used to collect the scattered signal dispersed on 1800 grooves/mm grating. The normal-incident transmittance spectra of the CZTS film were recorded by a double beam ultraviolet-infrared spectrophotometer (PerkinElmer Lambda 950) at the photon energy from 0.5 to 6.5 eV (190–2650 nm) with a spectral resolution of 2 nm. The film was mounted into a closed cycle refrigerator system (Janis SHI-4-1), where the temperature can be varied from 8 to 300 K. Note that the temperature dependent transmittance experiment of the sapphire substrate was carried out under the same conditions for deriving its dielectric function. To eliminate the effects from the windows of the cryostat, the transmittance spectra of the quartz windows were also recorded at the corresponding temperature.

3 Results and discussions

3.1 Structural and morphology characterizations

Fig. 1(a) shows the XRD pattern of the CZTS film. There are the diffraction peaks (112), (200), (211), (220), and (312) (PDF#26-0575). It indicates that the film is polycrystalline and exhibits the single kesterite phase. The (112)-oriented growth is observed to be dominant for the CZTS film. According to Scherrer's equation, the grain size is estimated to be about 10 nm from the (112) diffraction peak. Fig. 1(b) shows the AFM morphology of the CZTS film. The AFM image shows a smooth surface with uniform island-like topography and the surface roughness of about 3 nm is much

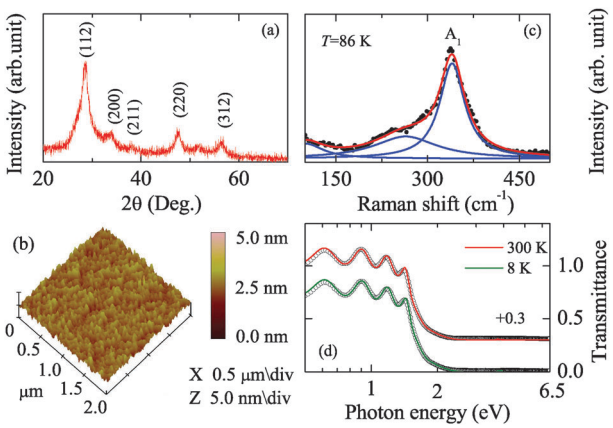

Fig. 1 (a) The X-ray diffraction pattern of the CZTS film at room temperature. (b) The AFM three-dimensional image. (c) Raman scattering spectra at 86 K. Note that the Lorentzian multipeak fitting is given by the solid lines. (d) Experimental (dot lines) and best fit (solid lines) transmittance spectra of the CZTS film at 8 and 300 K, respectively. The horizontal coordinate is the logarithmic unit to enlarge the transparent region.

smaller than that prepared by pulsed laser deposition.[7] From the results of AFM and XRD, it can be concluded that the film has a nanocrystalline growth pattern.

3.2 Lattice vibrations

The kesterite phase of CZTS has a space group of $I\bar{4}$, which consists of a ccp array of S atoms, with metal atoms occupying one half of the tetrahedral voids. For the kesterite phase materials, the group analysis predicts 21 optical phonon modes:[16–18] ($\Gamma_{\mathrm{Raman}} = 3A_1 + 6B + 6E_1 + 6E_2$). Here, B, E_1, and E_2 modes are infrared-active, while A_1, B, E_1, and E_2 modes are Raman-active modes. Fig. 1(c) displays the Raman scattering spectrum of the CZTS film at 86 K. In order to determine the peak positions of the phonon modes, a curve fitting of the Raman spectrum in the wavenumber range of 100–500 cm^{-1} was carried out. The Lorentzian multipeak fitting including three peak and shoulder structures at about 105, 263, and 340 cm^{-1} is required to describe the profile satisfactorily. These peak positions are close to the previously published results for the kesterite phase of CZTS.[19–21] The strongest peak can be attributed to the A_1 symmetry of kesterite CZTS.[21] The A_1 phonon mode is pure anion mode, which corresponds to the vibration of S atoms surrounded by motionless neighboring atoms.[22] Furthermore, the XRD and Raman results indicate the absence of phase separation and formation of binary phases within the experimental detection errors.

In order to observe the temperature effects on the lattice vibrations of the CZTS film, Raman spectra were collected in the temperature range from 86 K to 323 K and are shown in Fig. 2(a). It can be found that the A_1 phonon mode is strongly affected by the temperature. As we know, the evolution of phonon frequency and relative intensity with respect to temperature can provide further valuable insights regarding the anharmonicity of vibration. Fig. 2(b) presents the temperature dependence of the A_1 phonon frequency and the linearly fitting result. With increasing the temperature, the A_1 phonon

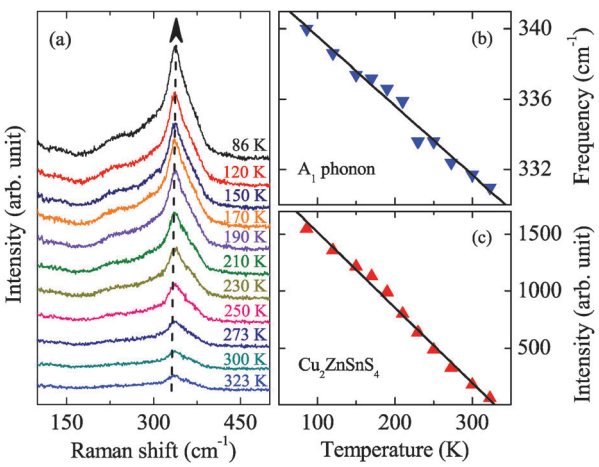

Fig. 2 (a) Raman spectra of the CZTS film with increasing temperatures from 86 K to 323 K. The dashed arrow is used to guide the eyes, which shows the variations of the peak position and relative intensity for the A_1 phonon mode with the temperature. (b) The A_1 phonon frequency variation as a function of temperature. (c) The temperature dependence of relative Raman scattering intensity for the A_1 phonon mode.

frequency linearly decreases from about 340 to 331 cm^{-1}. It suggests that the total red shift value of the phonon frequency is about 9 cm^{-1}, which is slightly larger than that reported by Sarswat *et al.* (4 cm^{-1}).[18] The fact that the A_1 phonon frequency shifts toward the lower energy side with the temperature can be ascribed to the combined effects of thermal expansion and the anharmonic coupling to other phonons.[23,24] In order to further characterize the variation of the phonon mode, the relative intensity of the A_1 Raman line after background signal subtraction is exhibited in Fig. 2(c). One can observe that the intensity of the vibration mode linearly decreases with increasing the temperature. This may be ascribed to the structural effects and lattice thermal effects, which result in the reduction of the vibration strength in S atoms surrounded by motionless neighboring atoms with the temperature.

3.3 Theoretical consideration for transmittance spectra

It is a challenge to simulate the transmittance spectrum of a semiconductor film in a wider photon energy region because there is a stronger parameter correlation if a complicated dielectric function model is applied. The inverse synthesis method is based on a phenomenological model fitted to the experimental results. The complex dielectric functions ($\varepsilon = \varepsilon_r + i\varepsilon_i$) of the CZTS film can be expressed using three Tauc–Lorentz (TL) oscillator model:[25,26]

$$\varepsilon_r(E) = \varepsilon_\infty + \frac{2}{\pi} P \int_0^\infty \frac{\xi \varepsilon_i(E)}{\xi^2 - E^2} \mathrm{d}\xi \quad (1)$$

$$\varepsilon_i(E) = \sum_{m=0}^{2} \frac{A_m E_{pm} \Gamma_m (E - E_{tm})^2}{(E^2 - E_{pm}^2)^2 + \Gamma_m^2 E^2} \frac{1}{E} \quad (2)$$

where ε_∞ is the high frequency dielectric constant, P is the Cauchy principal part of the integral, E is the incident photon energy, A_m, E_{pm}, Γ_m, and E_{tm} are the amplitude, peak position energy, broadening term, and Tauc gap energy of the mth oscillator, respectively.

The best-fit parameter values in eqn (1) and (2) can be found using a Levenberg–Marquardt algorithm, which is an efficient non-linear calculation method for many parameter fittings.[27] In the method, the fitted parameters are independent of each other and their standard errors are from the experimental uncertainty. The best-fit model is chosen by optimizing simultaneously the comparison between the experimental and calculated spectra, unbiased estimator for the difference between them, physical likelihood of the solution, 90% confidence limits on each fitting parameter, and correlation coefficient matrix describing the degree of interdependence between the parameters. The fitting is a process of minimizing error function with the optimized values of the fitting parameters. In addition, the dielectric function of the substrate should be required in order to model the transmittance spectra of the CZTS/sapphire multilayer structures.

As an example, the experimental and fitted transmittance spectra of the CZTS film at 8 and 300 K are shown in Fig. 1(d) with the dotted and solid lines, respectively. The interference oscillation patterns (due to the finite thickness of the film) can be observed at the photon energy below 1.5 eV, indicating that

Table 1 The Tauc–Lorentz parameter values of the CZTS film are determined from the simulation of transmittance spectra in Fig. 1(d) at 8, 150, and 300 K, respectively. Note that the ε_∞ is estimated to be 2.34 taken from the fitting result at room temperature

Oscillator	Parameters	8 K	150 K	300 K
$m = 0$	A_0	9.81	9.81	9.83
	E_{p0}	1.51	1.51	1.49
	Γ_0	0.60	0.60	0.60
	E_{t0}	1.42	1.42	1.41
$m = 1$	A_1	20.1	20.1	20.2
	E_{p1}	3.58	3.58	3.54
	Γ_1	0.85	0.85	0.85
	E_{t1}	1.40	1.40	1.39
$m = 2$	A_2	4.96	4.96	4.99
	E_{p2}	4.27	4.26	4.19
	Γ_2	2.89	2.89	2.88
	E_{t2}	0.77	0.77	0.76

the film is transparent in this region. Note that the absorption edge shifts toward a lower energy side with the temperature. It indicates that the OBG decreases with increasing the temperature and has a negative temperature coefficient. A good agreement is obtained between the experimental and calculated spectra in the entirely measured photon energy range, especially near the fundamental band gap region. The dielectric functions of the CZTS film can be uniquely determined by fitting the model function to the experimental data. The fitted parameter values at 8 K, 150 K, and 300 K are summarized in Table 1. It can be observed that the parameter A increases while the parameters E_p and E_t decreases with the temperature. The thickness of the CZTS film is estimated to 909 ± 1 nm by fitting the transmittance spectra recorded at room temperature (RT). Note that the high frequency dielectric constant ε_∞ is calculated to be 2.34 at RT. The value is slightly less than that of the theoretical prediction, which could be attributed to a low packing density and polycrystalline structure of the CZTS film.[5]

3.4 Dielectric functions

Fig. 3(a) shows the evaluated dielectric functions of the kesterite CZTS film at 8, 150, and 300 K, respectively. The real part ε_r increases with the photon energy and approaches the maximum,

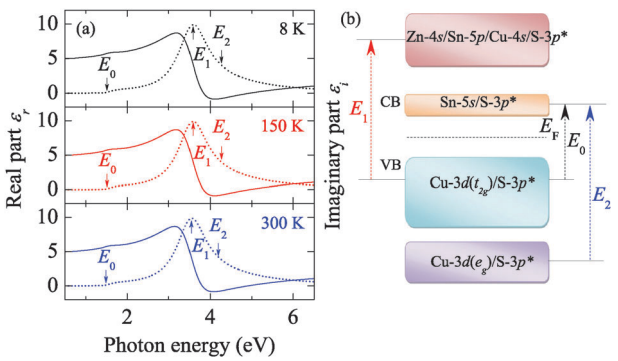

Fig. 3 (a) Real (ε_r) and imaginary (ε_i) parts of the dielectric functions for the CZTS film at 8, 150, and 300 K, respectively. The arrows indicate the energy positions of the electronic transitions. The solid lines and dot lines represent ε_r and ε_i, respectively. (b) The schematic diagram of electronic band structure and corresponding electronic transitions in the CZTS film.

then decreases with further increasing photon energy. For the imaginary part ε_i, the experimental result is in good agreement with that reported theoretically in the visible spectral range.[28] However, the ε_i displays a peak in the photon energy range of 3–4 eV. The number of optical transition is related to the physical properties of the CZTS film. Based on the theoretical calculations and experimental observations, three transitions at the photon energy from ultraviolet to near-infrared and the assignments are widely acceptable. For the present CZTS film, there are three thresholds in the ε_i spectra, located at about 1.5, 3.6, and 4.2 eV, respectively. With increasing the photon energy, the transitions are labeled as E_0, E_1, and E_2 in order. With increasing the temperature, both the real part ε_r and imaginary part ε_i shift toward a lower energy side. This is because the electronic orbital hybridization, band splitting, and atom interaction are strongly affected by the temperature, which results in the modification of electronic band structures. At the photon energy of 1.5 eV, the ε_r value was approximately varied from 5.345 to 5.396 for the temperature varied in the range of 8–300 K, which suggests that the refractive index n correspondingly increases from 2.312 to 2.323.

3.5 Electronic band structures and interband transitions

We will try to explain the three interband transitions according to the calculated density of states.[14,29] Fig. 3(b) shows the schematic diagram of the electronic band component and electronic transitions in the CZTS film. For the kesterite CZTS, the valence band (VB) is mainly made up of the antibonding component of the hybridization between Cu-3d states and S-3p states (Cu-3d/S-3p*).[5,14,29] Furthermore, the Cu-3d states are split into e_g and t_{2g} orbitals in the tetrahedral crystal field, which hybridize with S-3p states to create a lower and higher VB.[14] On the other hand, the Sn-5s and S-3p states hybridize (Sn-5s/S-3p) resulting in an occupied bonding state about 8 eV below the top of the VB, and an antibonding state (Sn-5s/S-3p*) making up the conduction band (CB).[14] The Sn-5p, Zn-4s, and Cu-4s orbitals are hybridized with S-3p, with the bonding states deep in the VB (below the Cu-3d/S-3p VB), and the antibonding states above the first Sn-5s/S-3p CB, acting as the second CB.[5,14]

Based on the theoretical calculations and experimental observations, the E_1 feature can be assigned to the transition from Cu-3d(t_{2g})/S-3p* states to Sn-5p/Zn-4s/Cu-4s/S-3p* states at the Γ point. It suggests that the E_1 transition corresponds to the electron transition between VB and the second CB. However, the E_2 assignment could be more complicated due to different origins from the theoretical investigations.[5,14,29] For example, the E_2 peak can be attributed to the transition from Cu-3d(e_{2g})/S-3p* states to Sn-5s/S-3p* states or to the transition from Cu-3d(t_{2g})/S-3p* states to Sn-5p/Zn-4s/Cu-4s/S-3p* states. Nevertheless, the calculated energies for both the transitions are much closer to the experimental data of about 4.2 eV.

It may be inaccurate to determine the OBG by the conventional linear extrapolated method owing to the small shift of the absorption edge and selected experimental range.[30] Fortunately, the OBG with the temperature can be directly determined by theoretical fitting to the transmittance spectra

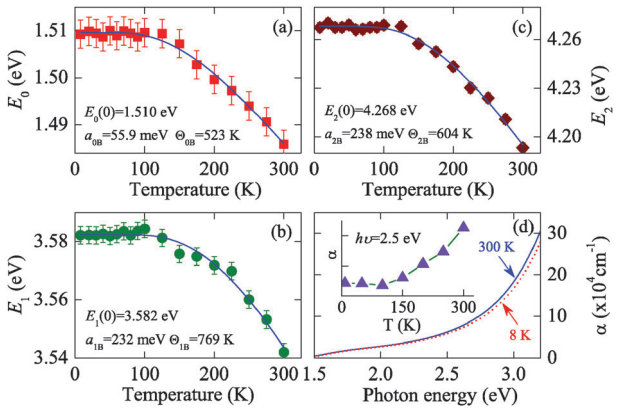

Fig. 4 The temperature dependence of electronic transition energies of (a) E_0, (b) E_1, and (c) E_2, respectively. The solid curves are the fitting results with the Bose–Einstein model. (d) The absorption coefficient of the CZTS film at 8 and 300 K, respectively. The inset shows the variation trend of the absorption coefficient with the temperature at the photon energy of 2.5 eV.

with the TL model. The E_0 transition could be related to the direct band gap at the Γ points in the Brillouin zone. Therefore, the parameter E_0 should be a response to a transition from the Cu-3$d(t_{2g})$/S-3p* states to the Sn-5s/S-3p* states. The E_0 transition energy is estimated to be 1.486 eV at RT, and the value is similar to that derived by the experimental and theoretical observations.[5,31] As can be seen in Fig. 4(a), the OBG energy decreases from 1.510 eV to 1.486 eV, corresponding to increasing the temperature from 8 to 300 K. For most semiconductors, the temperature dependence of the direct band gap, determined from the absorption edges, can be described by the Bose–Einstein model:[32,33]

$$E(T) = E_0(0) - \frac{2a_B}{\exp(\Theta_B/T) - 1} \qquad (3)$$

where, $E_0(0)$ is the OBG at 0 K, a_B is the strength of the coupling interaction, $\Theta_B \equiv \hbar\nu/k_B$ is the characteristic temperature representing the effective phonon energy on the temperature scale, and T is the experimental temperature. In principle, the agreement between the experimental and theoretical data is good with the model. The $E_0(0)$ value is estimated to be about 1.510 eV. The parameters a_B and Θ in eqn (3) are 56 meV and 523 K, respectively. The electron–phonon interaction and the lattice thermal expansion are responsible for the band gap narrowing with the temperature. In particular, the electron–phonon interaction, which includes the contributions from both acoustic as well as optical phonons, is usually the dominating one.[34–36] Note that the total energy shift of the E_0 transition is 23 meV, which indicates that band gap of the CZTS film is remarkably stable with the temperature. In contrast, the power conversion efficiency and the dark resistance of $Cu_2ZnSn(S,Se)$ solar cells are extremely sensitive to the temperature.[9] Therefore, one can conclude that the temperature effect on the OBG is rather small and could be neglected in the solar cell applications.

Fig. 4(b) and (c) show the temperature dependence of the E_1 and E_2 electronic transitions, respectively. With increasing the temperature, the E_1 transition energy shifts from 3.582 to 3.542 eV, while the obtained value of the E_2 transition is varied between 4.267 and 4.193 eV. The total energy shifts of the E_1 and E_2 transitions are 40 and 74 meV, respectively. The total energy shift of the E_2 transition is larger than that of the low level energy transitions. It indicates that the temperature has a greater effect on the higher level electronic transition. Note that both the variation trend of the E_1 and E_2 transition energy also can be described by the Bose–Einstein model, as can be seen in Fig. 4(b) and (c). Correspondingly, the band gap energy narrowing coefficient ($\beta = dE_0/dT$) of the kesterite CZTS film is calculated to be -1.66×10^{-4} eV K^{-1}, which agrees with the results for most semiconductors reported.[33] The negative β value indicates that the relative position of the valence band and the conduction band shifts with increasing the temperature.

3.6 Absorption coefficient

For absorber layer materials, the absorption coefficient ($\alpha = 4\pi k/\lambda$) is one of the most important parameters for their photovoltaic applications. To clarify the properties, the absorption coefficient of the CZTS film at 8 and 300 K are presented in Fig. 4(d). The order of magnitude is calculated to be about 10^5 cm^{-1} in the visible light region, which is similar to the values obtained theoretically and experimentally.[5,37] The large value of the absorption coefficient is an advantage for the band-edge absorption efficiency in CZTS-based solar cells. Considering the energy region absorbed by the solar cell is typically less than 3 eV,[14] the E_1 and E_2 electronic transitions make a tiny contribution to the absorption. Therefore, the most relevant transition for photovoltaic applications is the electron excitation from the Cu-3$d(t_{2g})$/S-3p* band to the Sn-5s/S-3p* band (see Fig. 3). The inset of Fig. 4(d) shows the variation trend of absorption coefficient with the temperature at the photon energy of 2.5 eV. It indicates that the α value increases from 5.89×10^4 to 6.25×10^4 cm^{-1}, corresponding to increasing the temperature from 8 to 300 K. The phenomena could be attributed to the decrease of the electronic transition energy with the temperature, which results in more photons being absorbed.

Due to the similarity between the photovoltaic CZTS and CZTSe compounds, it is interesting to make a comparison of the optical response behavior. Now, one can safely conclude that the CZTS material has a direct band gap of about 1.5 eV at RT. Compared to the CZTSe, the present CZTS has an obvious advantage in solar cell devices. It was reported from the first principles calculations that the chemical potential range for the CZTS formation without the secondary phases is very small.[8,29] Therefore, it is necessary to avoid the formation of ZnS precipitates to fabricate the CZTS compound. As we know, ZnS has a wide band gap energy of about 3.5 eV at RT.[38] From the above XRD and Raman analysis (see Fig. 1), the ZnS impurity phase does not exist in the present CZTS film, as compared to the reported results.[21] Otherwise, the band gap will increase and the case is similar to the ZnSe appearance in the CZTSe material.[39] That is to say, the OBG value of the CZTS film is intrinsic by studying the high quality material, which confirms the theoretical data and clarifies the argument. On the other hand, the longitudinal

optical (LO) phonon energy of the CZTS film is estimated to about 41 meV observed by Raman scattering spectra, which is slightly smaller than that from the CZTSe film (28 meV).[40] It indicates that the phonon replicas and excitonic effect become stronger in the CZTS film. To clarify the phenomena, the photoluminescence experiments at low temperature are requisite to analyze the temperature quenching. Nevertheless, the present investigations provide a critical judgment on the band gap and higher-energy electronic transitions of the CZTS material, which are helpful to optimize CZTS-based photovoltaic devices.

4 Conclusions

In summary, the A_1 phonon frequency of the kesterite CZTS film from Raman spectra linearly decreases from about 340 to 331 cm^{-1} with increasing the temperature from 86 to 323 K. The dielectric functions, optical band gap, and interband electronic transitions of the film have been investigated using ultraviolet-infrared transmittance spectra in the temperature range of 8–300 K. There are three electronic transitions, which can be readily assigned to the transitions from the Cu-3*d*(t_{2g})/S-3*p** states to the Sn-5*s*/S-3*p** states, Cu-3*d*(t_{2g})/S-3*p** states to Sn-5*p*/Zn-4*s*/Cu-4*s*/S-3*p** states, and Cu-3*d*(e_{2g})/S-3*p** states to Sn-5*s*/S-3*p** states, respectively. The optical band gap is estimated to be about 1.486 eV at room temperature and has a negative temperature coefficient.

Acknowledgements

This work was financially supported by Natural Science Foundation of China (Grant Nos. 60906046 and 11074076), Major State Basic Research Development Program of China (Grant No. 2011CB922200), Program of New Century Excellent Talents, MOE (Grant No. NCET-08-0192), Projects of Science and Technology Commission of Shanghai Municipality (Grant Nos. 10DJ1400201, 11520701300, and 10SG28), and The Program for Professor of Special Appointment (Eastern Scholar) at Shanghai Institutions of Higher Learning. One of authors (Wenwu Li) thanks the projects from ECNU (Grant Nos. PY2011014 and MXRZZ2011010).

References

1 J. Ajuria, I. Etxebarria, E. Azaceta, R. Tena-Zaera, N. Fernández-Montcada, E. Palomares and R. Pacios, *Phys. Chem. Chem. Phys.*, 2011, **13**, 20871–20876.
2 C. Steinhagen, M. G. Panthani, V. Akhavan, B. Goodfellow, B. Koo and B. A. Korgel, *J. Am. Chem. Soc.*, 2009, **131**, 12554–12555.
3 T. K. Todorov, K. B. Reuter and D. B. Mitzi, *Adv. Mater.*, 2010, **22**, E156–E159.
4 K. Wang, B. Shin, K. B. Reuter, T. Todorov, D. B. Mitzi and S. Guha, *Appl. Phys. Lett.*, 2011, **98**, 051912.
5 C. Persson, *J. Appl. Phys.*, 2010, **107**, 053710.
6 F. Liu, Y. Li, K. Zhang, B. Wang, C. Yan, Y. Lai, Z. Zhang, J. Li and Y. Liu, *Sol. Energy Mater. Sol. Cells*, 2010, **94**, 2431–2434.
7 L. Sun, J. He, H. Kong, F. Y. Yue, P. X. Yang and J. H. Chu, *Sol. Energy Mater. Sol. Cells*, 2011, **95**, 2907–2913.
8 S. Y. Chen, A. Walsh, J. H. Yang, X. G. Gong, L. Sun, P. X. Yang, J. H. Chu and S. H. Wei, *Phys. Rev. B: Condens. Matter Mater. Phys.*, 2011, **83**, 125201.
9 O. Gunawan, T. K. Todorov and D. B. Mitzi, *Appl. Phys. Lett.*, 2010, **97**, 233506.
10 H. Katagiri, K. Jimbo, S. Yamada, T. Kamimura, W. S. Maw, T. Fukano, T. Ito and T. Motohiro, *Appl. Phys. Express*, 2008, **1**, 041201.
11 W. Shockley and H. J. Queisser, *J. Appl. Phys.*, 1961, **32**, 510–519.
12 K. Wang, O. Gunawan, T. Todorov, B. Shin, S. J. Chey, N. A. Bojarczuk, D. Mitzi and S. Guha, *Appl. Phys. Lett.*, 2010, **97**, 143508.
13 H. Yoo and J. Kim, *Sol. Energy Mater. Sol. Cells*, 2011, **95**, 239–244.
14 J. Paier, R. Asahi, A. Nagoya and G. Kresse, *Phys. Rev. B: Condens. Matter Mater. Phys.*, 2009, **79**, 115126.
15 S. C. Riha, B. A. Parkinson and A. L. Prieto, *J. Am. Chem. Soc.*, 2011, **133**, 15272–15275.
16 M. Himmrich and H. Haeuseler, *Spectrochim. Acta*, 1991, **47A**, 933–942.
17 M. I. Aroyo, J. M. Perez-Mato, C. Capillas, E. Kroumova, S. Ivantchev, G. Madariaga, A. Kirov and H. Wondratschek, *Z. Kristallogr.*, 2006, **221**, 15–27.
18 P. K. Sarswat, M. L. Free and A. Tiwari, *Phys. Status Solidi B*, 2011, **248**, 2170–2174.
19 P. A. Fernandes, P. M. P. Salomé and A. F. da Cunha, *J. Alloys Compd.*, 2011, **509**, 7600–7606.
20 M. Altosaar, J. Raudoja, K. Timmo, M. Danilson, M. Grossberg, J. Krustok and E. Mellikov, *Phys. Status Solidi A*, 2008, **205**, 167–170.
21 X. Fontané, L. Calvo-Barrio, V. Izquierdo-Roca, E. Saucedo, A. Pérez-Rodriguez, J. R. Morante, D. M. Berg, P. J. Dale and S. Siebentritt, *Appl. Phys. Lett.*, 2011, **98**, 181905.
22 H. Neumann, *Helv. Phys. Acta*, 1985, **58**, 337–346.
23 H. Tang and I. P. Herman, *Phys. Rev. B: Condens. Matter*, 1991, **43**, 2299–2304.
24 J. Menéndez and M. Cardona, *Phys. Rev. B*, 1984, **29**, 2051–2059.
25 J. G. E. Jellison and F. A. Modine, *Appl. Phys. Lett.*, 1996, **69**, 371–373; 1996, **69**, 2137.
26 W. L. Yu, K. Jiang, J. D. Wu, J. Gan, M. Zhu, Z. G. Hu and J. H. Chu, *Phys. Chem. Chem. Phys.*, 2011, **13**, 6211–6222.
27 W. H. Press, S. A. Teukolsky, W. T. Vetterling and B. P. Flannery, *Numerical Recipes in C: The Art of Scientific Computing*, Cambridge University Press, Cambridge MA, 1992.
28 Y. T. Zhai, S. Y. Chen, J. H. Yang, H. J. Xiang, X. G. Gong, A. Walsh, J. Kang and S. H. Wei, *Phys. Rev. B: Condens. Matter Mater. Phys.*, 2011, **84**, 075213.
29 S. Y. Chen, X. G. Gong, A. Walsh and S. H. Wei, *Appl. Phys. Lett.*, 2009, **94**, 041903.
30 W. W. Li, J. J. Zhu, J. D. Wu, J. Sun, M. Zhu, Z. G. Hu and J. H. Chu, *ACS Appl. Mater. Interfaces*, 2010, **2**, 2325–2332.
31 L. Shi, C. Pei, Y. Xu and Q. Li, *J. Am. Chem. Soc.*, 2011, **133**, 10328–10331.
32 L. Viña, S. Logothetidis and M. Cardona, *Phys. Rev. B*, 1984, **30**, 1979–1991.
33 W. W. Li, J. J. Zhu, X. F. Xu, K. Jiang, Z. G. Hu, M. Zhu and J. H. Chu, *J. Appl. Phys.*, 2011, **110**, 013504.
34 S. Biernacki, U. Scherz and B. Meyer, *Phys. Rev. B: Condens. Matter*, 1994, **49**, 4501–4510.
35 S. A. Lourenço, I. F. L. Dias, J. L. Duarte, E. Laureto, E. A. Meneses, J. R. Leite and I. Mazzaro, *J. Appl. Phys.*, 2001, **89**, 6159–6164.
36 W. W. Li, J. J. Zhu, J. D. Wu, J. Gan, Z. G. Hu, M. Zhu and J. H. Chu, *Appl. Phys. Lett.*, 2010, **97**, 121102.
37 Y. B. Kishore Kumar, G. Suresh Babu, P. Uday Bhaskar and V. Sundara Raja, *Sol. Energy Mater. Sol. Cells*, 2009, **93**, 1230–1237.
38 D. J. Kim, Y. M. Yu, Y. D. Choi, J. W. Lee and C. S. Kim, *Appl. Phys. Lett.*, 2006, **88**, 051902.
39 S. Ahn, S. Jung, J. Gwak, A. Cho, K. Shin, K. Yoon, D. Park, H. Cheong and J. H. Yun, *Appl. Phys. Lett.*, 2010, **97**, 021905.
40 F. Luckert, D. I. Hamilton, M. V. Yakushev, N. S. Beattie, G. Zoppi, M. Moynihan, I. Forbes, A. V. Karotki, A. V. Mudryi, M. Grossberg, J. Krustok and R. W. Martin, *Appl. Phys. Lett.*, 2011, **99**, 062104.